

Submitted to *Astronomy Letters*

THE ERUPTIVE YOUNG STAR IRAS 21204+4913

M. A. Burlak,¹ A. V. Dodin,¹ A. V. Zharova,¹ S. G. Zheltoukhov,¹ N. P. Ikonnikova,¹ S. A. Lamzin,^{1,*} B. S. Safonov,¹ I. A. Strakhov,¹ A. A. Tatarnikov,¹ and A. M. Tatarnikov¹

¹*Sternberg Astronomical Institute, M.V. Lomonosov Moscow State University, Moscow, 119234 Russia*

The results of photometric, polarimetric, and spectroscopic observations are presented for the young star IRAS 21204+4913, whose visible brightness has increased by $\approx 5^m$ since October 2025. The star's absorption spectrum in the $0.36 - 0.75 \mu\text{m}$ range resembles those of A-F giants and supergiants, but it also exhibits molecular TiO bands. The brightening was accompanied by a significant increase in the degree of polarization of the stellar radiation (to $\approx 16\%$ in the *I*-band), likely due to scattering by dust in an expanding circumstellar shell. The P Cygni profile of the $\text{H}\alpha$ line implies a dusty wind velocity of $\approx 300 \text{ km s}^{-1}$. We believe that the outburst of IRAS 21204+4913 is caused by an increase in the accretion rate of protoplanetary disk's matter onto the young star with a mass of $\lesssim 0.5 \text{ M}_\odot$ to $\gtrsim 3 \times 10^{-5} \text{ M}_\odot \text{ yr}^{-1}$. Furthermore, IRAS 21204+4913 displays several unusual features: the dependence of the width and radial velocity of absorption lines on the excitation potential, emission in the TiO molecular bands, and a comparably bright outburst that occurred in 1948. Several T Tauri stars and a group of Herbig-Haro objects are found in the vicinity of the star.

Keywords: stars: pre-main-sequence star — stars: individual: IRAS 21204+4913, Gaia DR3 2171042269468334080, Gaia DR3 2171089101807867520 — stars: activity

1. INTRODUCTION

During the transformation of a protostellar cloud into a T Tauri star — a process lasting ~ 0.5 Myr — some young stellar objects (YSOs) undergo dramatic brightening events that can persist from several months to several decades (Herbig 1977). It is generally accepted that outbursts of this kind are caused by a strong increase in the accretion rate \dot{M}_{ac} of protoplanetary disk matter onto the forming star (Audard et al. 2014, Hartmann et al. 2016, Hartmann and Kenyon 1996). In extreme cases, \dot{M}_{ac} can exceed $10^{-4} \text{ M}_\odot \text{ yr}^{-1}$, which is thousands of times more than typical \dot{M}_{ac} observed in classical T Tauri stars (CTTSs). If such events recur frequently during star formation, they may significantly influence the final stellar mass and other fundamental parameters of the star — see Baraffe et al. (2017), Fischer et al. (2023) and references therein. A strong, albeit relatively short-term, increase in the luminosity of YSOs undoubtedly influences the evolution of their protoplanetary disks, and therefore the formation of planetary

systems — see, e.g., Stamatellos et al. (2012), Topchieva et al. (2025).

Various mechanisms have been proposed to explain the origin of powerful episodic accretion. Without aiming for completeness (see e.g. Fischer et al. 2023), we mention only a few: thermal, gravitational, and/or magnetorotational disk instabilities (Bae et al. 2014, Kadam et al. 2020, Meyer et al. 2017, Zhu et al. 2010); interactions between the disk and a planet or stellar companion (Borchert et al. 2022, Nayakshin et al. 2023); an infall of gas cloud onto the disk (Demidova and Grinin 2023).

Depending on the outburst amplitude, duration, and spectral characteristics, Herbig (1977) divided eruptive YSOs into two classes: FU Orionis-type objects — FUors¹ and EX Lupi-type objects — EXors (Herbig 1989). Herbig classified FUors as objects whose visible brightness increased by $4^m - 6^m$ over several months and then gradually decreased over several decades, and whose spectra were almost entirely absorption-dominated throughout the out-

* lamzin@sai.msu.ru

¹ The term *fuor* was introduced by V. A. Ambartsumyan (1971).

burst. EXors, in contrast, exhibit recurrent outbursts – sometimes reaching FUor-like amplitudes but lasting only weeks to a year – during which their spectra are dominated by emission lines.

Over the past decade, the advent of numerous monitoring systems has led to the discovery of a large number of eruptive YSOs. A team of researchers Contreras Peña et al. (2025) compiled the OYCAT (Outbursting YSOs Catalogue)², which currently contains basic information on 174 objects. According to the established criteria (Contreras Peña et al. 2025, table 1), the objects in the catalogue are divided into several groups based on the photometric and spectral characteristics of their outbursts. Without going into detail, we note that the authors confidently classified as FUors and EXors fewer than 40% of all objects, whereas nearly half of the YSOs exhibited outburst parameters intermediate between those of FUors and EXors.

The diversity of observed manifestations of episodic accretion can be attributed either to different underlying physical mechanisms or to the combined action of multiple mechanisms – see, for example, Skliarevskii and Vorobyov (2023). Acquiring the most comprehensive possible information on each eruptive YSO will help elucidate the general physics of the phenomenon. In this context, we became interested in the report by S. Kaneko³, who discovered on November 25, 2025, the optical transient TCP J21220926+4926242 (hereafter J2122), whose brightness in the optical band approximately doubled over the following week.

Subsequently, it became clear that the outburst occurred no later than October 25, 2025, when the transient was first detected by the ASAS-SN survey (Shappee et al. 2014) at a magnitude of $g = 16^m9$ (Kochkina et al. 2025). By late November, when the brightness of J2122 exceeded $V \approx 12^m4$, Kochkina et al. (2025) carried out the first spectroscopic observations of the transient in the wavelength range of

$0.36 - 0.72 \mu\text{m}$ and found that its spectrum resembled the absorption-dominated spectra typical of FUor-like objects: the only emission feature detected in the spectrum of J2122 was the [S II] 6731 Å line.

Grosso et al. (2025) identified the transient J2122 with the IRAS source 21204+4913 (Neugebauer et al. 1984), which, according to Marton et al. (2016), is a class I/II YSO – i.e., it is in the transitional evolutionary stage between a protostar and a pre-main-sequence star (Adams et al. 1987, Lada 2005). IRAS 21204+4913 lies on the southeastern edge of the relatively compact (18 square arcminutes) dark nebula D 2944 (Dobashi 2011). Grosso et al. (2025) determined a distance to the source of ≈ 500 pc, and Stecklum (2025) reported a line-of-sight extinction of $A_V \approx 8^m$.

We began observing IRAS 21204+4913 in early December 2025, and in this paper we present the results of our research. First, we describe our observational data and the results derived from them; then, we examine what our data reveal about the nature of IRAS 21204+4913. The conclusions and main findings of this work are summarized in the Conclusion.

2. OBSERVATIONS

To construct the historical light curve of IRAS 21204+4913, we selected approximately 100 photographic plates from the collection of the Sternberg Astronomical Institute of Lomonosov Moscow State University (SAI MSU) that included the star. These plates were obtained between May 10, 1899, and November 7, 1975, in a photometric system close to the Johnson B band. The limiting magnitude of the plates varied from $B \approx 14^m$ to 18^m , depending on the instrument used and the observing conditions.

The observations presented below were carried out in 2025–2026 with the instruments of the Caucasian Mountain Observatory (CMO) of SAI MSU (Shatsky et al. 2020). Optical photometry of IRAS 21204+4913 was obtained with the 60-cm RC600 telescope equipped with a CCD camera and a set of $UBVR_cI_c$ filters in the Bessell-

² <http://starformation.synology.me:5002/OYCAT/main.html>

³ <https://www.astroarts.co.jp/photo-gallery/photo/129147>

Cousins photometric system (Berdnikov et al. 2020). The magnitudes of the comparison stars were calibrated against the standard field GD391 (Clem and Landolt 2016). The results of the optical photometry are presented in Table A1.

Photometric observations of the star in the near-infrared (NIR) were carried out in the *YJHK* bands of the MKO-NIR photometric system using the ASTRONIRCAM infrared camera-spectrograph (Nadip et al. 2017) mounted on the 2.5-m telescope. A detailed description of the observational procedure and data reduction can be found in Tatarnikov et al. (2023). The following stars from the 2MASS catalogue were used as photometric standards: 2MASS J21222481+4927597, 2MASS J21220594+4925335, and 2MASS J21222134+4925561. Their magnitudes were transformed into the MKO-NIR system using the color-term equations provided in Tatarnikov and Tatarnikov (2023). Additionally, we observed the source in the L' ($\lambda_c = 3.8 \mu\text{m}$) and M' ($\lambda_c = 4.7 \mu\text{m}$) bands – close to the corresponding MKO-NIR bands – using the LMP camera (Zheltoukhov et al. 2024). Photometric reference stars from the list of Shenavrin et al. (2011), positioned at the same airmass as the target during the observations, were employed as comparison stars. The results of our NIR photometry are presented in Table A2.

Polarimetric observations in the BVR_cI_c bands were carried out with the 2.5-m telescope using the speckle polarimeter (Safonov et al. 2017). The instrument is a dual-beam polarimeter equipped with a rotating half-wave plate as the modulator and a polarizing beamsplitting cube as the beamsplitter. The primary detector is a fast, low-noise CMOS camera (Hamamatsu ORCA-Quest). For each photometric band, we obtained a series of 4000 frames, each with an exposure time of 60 ms. During the acquisition, the half-wave plate rotated continuously at an angular velocity of 60°s^{-1} .

The acquired images were corrected for bias offset and demodulated using the known position angle of the half-wave plate for each frame. Aperture photometry was then performed on the resulting demodulated series, taking into account the possible contribution from polarized back-

ground emission. The resulting flux measurements were used to estimate the Stokes parameters in the instrumental reference frame. Transformation to the equatorial reference frame and correction for instrumental polarization of the telescope (observations were carried out in the Nasmyth-2 focus) were performed following the procedure described in Safonov et al. (2017). The results are presented in Table A3 and Fig. 4.

Low-resolution spectra of IRAS 21204+4913 were obtained with the Transient Double-beam Spectrograph (TDS). A detailed description of the instrument and the data reduction procedure can be found in Potanin et al. (2020). Here we only note that the spectral resolving power $R = \lambda/\Delta\lambda$ of the TDS is ≈ 1300 in the red channel ($0.56 - 0.74 \mu\text{m}$) and ≈ 2400 in the blue channel ($0.36 - 0.56 \mu\text{m}$) (Belinski et al. 2023).

High-resolution spectra (HRS, $R \sim 20\,000$ over the wavelength range $4050 - 8300 \text{ \AA}$) were obtained with the “Raduga” spectrograph – an échelle fiber-fed spectrograph with a fiber diameter of $2''5$. Data reduction was performed in the standard manner. Wavelength calibration was carried out using a hollow-cathode lamp (HCL). Spectral extraction followed the method described in Bolton and Schlegel (2010), employing HCL emission lines to construct a two-dimensional instrumental line-spread function. The high spatial resolution of the detector (9566×6388 pixels) enables sufficiently detailed modeling of the line profile to solve the inverse problem of spectrum extraction. Wavelength calibration frames were acquired immediately before and after each science exposure, and the dispersion solution was interpolated to the mid-exposure time of the science frame. Stability tests using radial velocity standard stars (HIP 43726 and HIP 17378) showed that the local calibration accuracy is approximately $\sigma = 0.4 \text{ km s}^{-1}$ – this represents the scatter of individual spectral lines in the Raduga spectra relative to a reference spectrum obtained with the ESPRESSO spectrograph (Pepe et al. 2021) at $R \sim 190\,000$. The random scatter in the mean radial velocities of the standard stars observed on different nights is $\sigma \approx 0.03 \text{ km s}^{-1}$.

All wavelengths and observation times for both spectrographs have been corrected to the

Table 1. Log of spectroscopic observations

date	object	BJD 246...	exposure sec.	PA °
HRS				
2025-12-04	0	1014.23	3600	-
2025-12-06	0	1016.15	3600	-
2025-12-08	0	1018.28	3600	-
2025-12-19	0	1029.25	7200	-
2026-01-02	0	1043.21	7200	-
TDS				
2025-12-04	0	1014.26	600	70.8
2025-12-06	0	1016.18	600	85.7
2025-12-18	0	1028.19	1800	-32.0
2025-12-18	0	1028.17	1800	148.0
2026-01-03	0	1044.19	600	67.5
2025-12-20	1	1030.25	600	91.5
2026-01-29	1	1070.19	2400	56.7
2025-12-20	2	1030.25	600	91.5
2025-12-18	HH	1028.23	900	158.0

The object designations follow those in Fig. 1. HH denotes Herbig-Haro objects.

barycenter of the Solar System. The log of spectral observations is presented in Table 1.

On December 3, 2025, we also obtained images of the IRAS 21204+4913 surroundings using the 4K×4K CCD camera mounted on the 2.5-m telescope. Observations were carried out in the H α filter ($\lambda_c = 656$ nm, $W = 7.7$ nm, a total exposure time of $\Delta t = 100$ min), and in the adjacent continuum filter Habc ($\lambda_c = 643$ nm, $W = 12$ nm, $\Delta t = 50$ min).

3. RESULTS

3.1. Image of the surroundings of IRAS 21204+4913 in the H α line

Fig. 1 shows the difference image of the IRAS 21204+4913 surroundings obtained in the Halp and Halpbc filters. IRAS 21204+4913 is marked in the figure as object 0 at the southeastern edge of the dark cloud D 2944. On the southern and southwestern edges of the same cloud, approximately 50'' and 2'27 west of IRAS 21204+4913, lie two stars that appear as bright spots, indicating strong H α emission in their spectra (see also Barentsen et al. 2014). These stars – Gaia DR3 2171042269468334080 and Gaia DR3 2171089101807867520 – are la-

beled in Fig. 1 as objects 1 and 2, respectively. Hereafter, we refer to them as stars S1 and S2.

As can be seen from Fig. 1, a group of emission nebulae adjoins the northern part of the dark cloud D 2944. These nebulae lie in the direction $PA_{HH} \approx -25^\circ$ from IRAS 21204+4913 at the projected distance of $d_{HH} \sim 2'5$. According to the spectrum shown in Fig. 2, the brighter, irregularly shaped nebulae – presumably Herbig-Haro (HH) objects – are superimposed on an extended emission background. The spectra of the background gas and the HH objects differ in two key respects. First, the [N II] doublet lines are present in the spectrum of the background gas but absent in that of the HH objects. Second, the barycentric radial velocity of the background gas is $V_r^{bg} \approx -40$ km s $^{-1}$, whereas that of the brighter clumps is $V_r^{HH} \approx -60$ km s $^{-1}$. In both the background and HH spectra, the [S II] $\lambda 6716$ Å line is significantly stronger than the $\lambda 6731$ Å line, implying an electron density $N_e \lesssim 200$ cm $^{-3}$ in the line-emitting regions (Proxauf et al. 2014).

3.2. Photometry

Fig. 3 shows the evolution of the brightness of IRAS 21204+4913 in the optical and NIR bands during our observation period, along with several of its color indices. It is evident that the rapid brightening in the optical (by nearly 5^m during November 2025; Stecklum 2025) slowed down significantly in December and essentially ceased by January. Throughout our monitoring period, the source's brightness variations from 0.37 to 4.8 μ m occurred nearly simultaneously. More precisely, after December 10, 2025, the color indices $U - B \approx -0.08$ and $B - V \approx +0.63$ remained constant within the photometric uncertainties, while the $V - I$ color initially decreased slightly and then stabilized.

3.3. Polarimetry

It follows from Table A3 and Fig. 4 that the emission from IRAS 21204+4913 is strongly polarized in the *BVRI* bands. At each epoch,

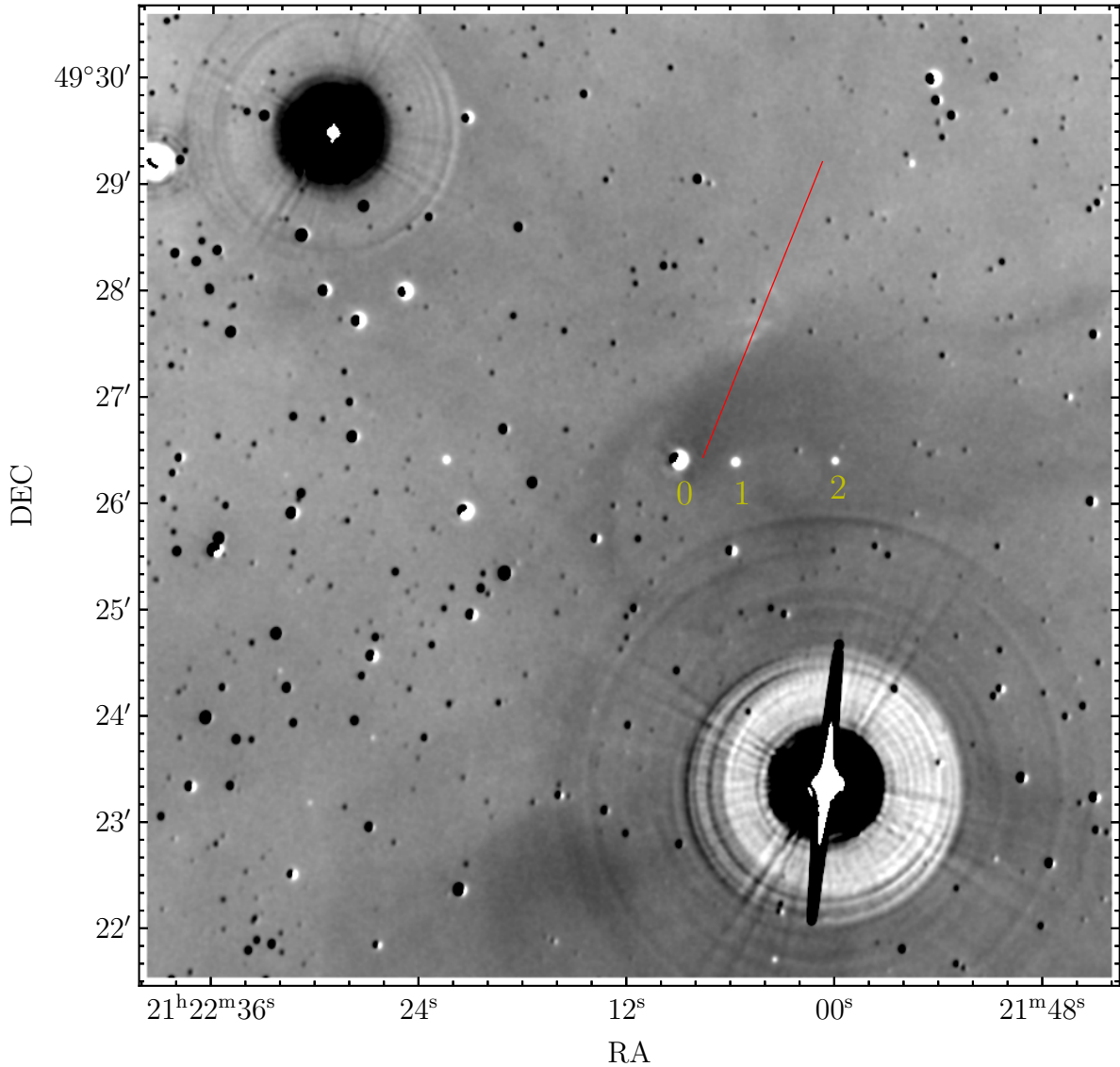


Figure 1. Difference image of the IRAS 21204+4913 surroundings in the Halp and Halpbc filters. Objects 0, 1, and 2 mark IRAS 21204+4913, star S1, and star S2, respectively. The red line segment passing through the Herbig-Haro objects (bright spots) indicates the position of the TDS spectrograph slit used to obtain the spectrum shown in Fig. 2. Further details are given in the text.

the degree of polarization p increases with wavelength λ , while the polarization angle $\theta(\lambda)$ is constant within the measurement uncertainties. During the course of our observations, the degree of polarization in the VRI bands increased, reaching $p \approx 16\%$ in the I band. The polarization angle θ also appears to have increased slightly during the observation period. This conclusion is quantitatively supported by a weighted least-squares fit (weights $1/\sigma_\theta^2$) to the time de-

pendence $\theta = kt + \theta_0$, which yields a slope k that differs from zero at the level of $\approx 5\sigma_k$.

3.4. Spectra

Fig. 5 shows low-resolution spectra of IRAS 21204+4913 obtained with TDS on different dates. Overall, the spectrum of the star resembles those of FUors (Fischer et al. 2023): it is dominated by absorption features, includ-

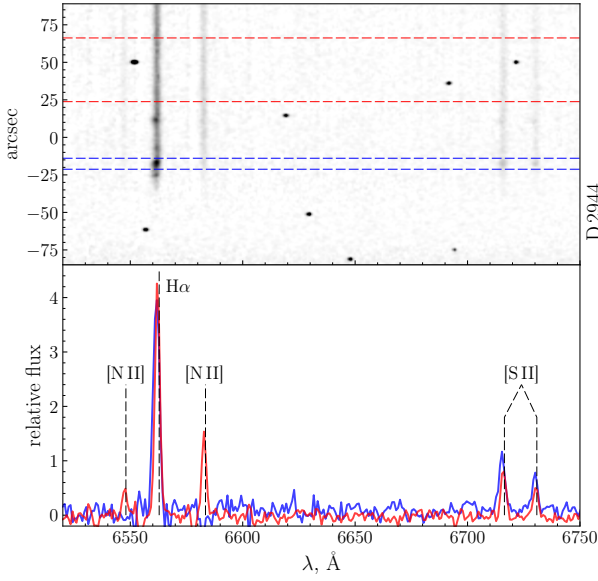


Figure 2. 2D (upper panel) and 1D (lower panel) TDS spectra of the emission nebulae located along the northern boundary of the dark cloud D 2944. The red curve shows the spectrum of the background nebula within the region bounded by the red dashed lines, while the blue curve represents the spectrum of the brightest clump (within the blue dashed lines) with the background spectrum subtracted. Scattered black dots in the 2D image are cosmic-ray hits.

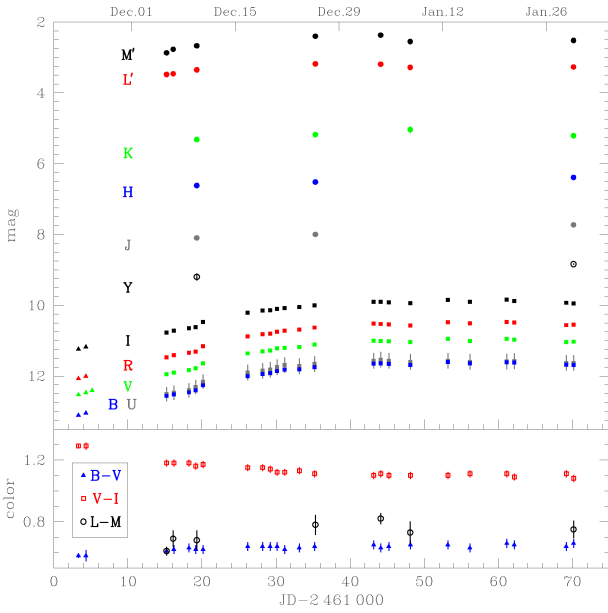


Figure 3. Variation of the brightness and selected color indices of IRAS 21204+4913 in the optical and NIR bands. Data obtained prior to December 10, 2025 are taken from Kochkina et al. (2025).

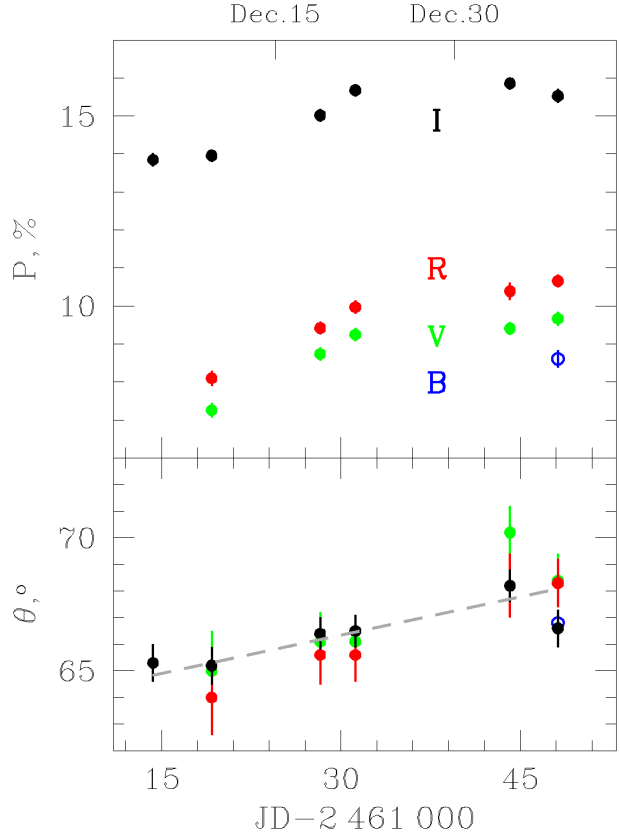


Figure 4. Evolution of the degree of polarization p and polarization angle θ of the radiation from IRAS 21204+4913. The gray dashed line shows the least-squares fit.

ing the Li I 6708 Å line, and exhibits both high-excitation atomic lines (e.g. He I , O I , Si II) and molecular TiO bands.

Another distinctive feature of the IRAS 21204+4913 spectrum that makes it resemble those of FUors (Fischer et al. 2023, Herbig 1975) is the presence, in the blue wing of certain strong lines – particularly $\text{H}\alpha$ (see Fig. 6) – of an extended absorption component. This fact indicates that the star, like FUors, has a gas shell that expands at velocities of $250 - 300 \text{ km s}^{-1}$, i.e., a wind.

Nevertheless, the spectrum of IRAS 21204+4913 exhibits features that are atypical for FUors. First, as seen in Fig. 5, the TiO molecular bands appear in emission rather than absorption. Second, there is a clear dependence both of the line width and radial velocity on the excitation energy (Fig. 7) – a behavior not previously observed in classical

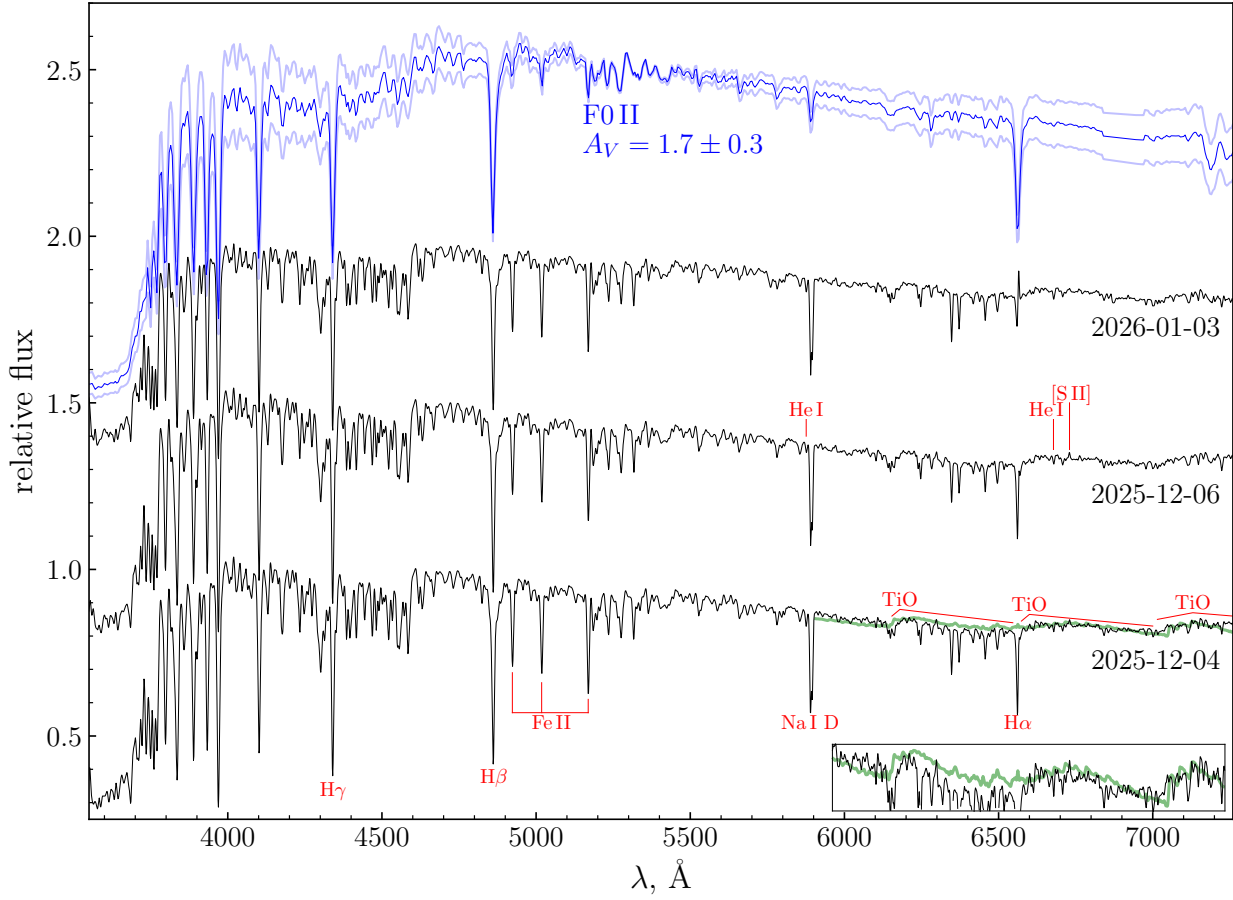


Figure 5. Low-resolution spectra of IRAS 21204+4913 (black lines). The blue lines show the spectrum of an F0 II star reddened by $A_V = 1.7 \pm 0.3$. In the red part of the IRAS 21204+4913 spectrum, broad emission-like “humps” are present, which can be interpreted as TiO bands in emission. For comparison, the green line shows the inverted and scaled spectrum of the M-type star HD 211029; the same spectral regions are displayed at an enlarged scale in the insert.

FUors, to the best of our knowledge.

The IRAS 21204+4913 spectrum exhibits several emission features. Firstly, as can be seen in Fig. 7, an emission component is present in the $H\alpha$ line profile in all the spectra obtained by us. Furthermore, two emission lines are visible in the stellar spectrum: $[S\,II]$ 6731 Å (see Fig. 5) and $[Ca\,II]$ 7291 Å. However, both are very weak, and the profile of the latter, as well as that of the $[S\,II]$ 6716 Å line, is distorted by a neighboring absorption feature. Therefore, we refrain from analyzing the detailed shapes of these lines, although we can state that the radial velocities of their centroids is $V_r < 0$. We also note that the $[O\,I]$ 5577, 6300, and 6363 Å lines present in the IRAS 21204+4913 spectrum are of telluric origin. Another emission feature, observed in all spectra

of the star near $\lambda \approx 6516$ Å (Fig. 8), probably corresponds to the fluorescent $Fe\,II]$ 6516.08 Å line.⁴ To the best of our knowledge, this line has not been previously reported in the spectra of FUors, although it is present in the spectra of some CTTS, e.g., RW Aur (Dodin et al. 2012).

3.5. Radial velocity estimation

In the previous section we showed that the radial velocity of IRAS 21204+4913 varies with the excitation potential of the spectral lines. To

⁴ Transition $a^6S_{5/2} - z^6D_{7/2}^o$, whose upper level is pumped by radiation from the $a^6D_{9/2, 7/2, 5/2}$ levels of the ground configuration of Fe II (Kramida et al. 2024).

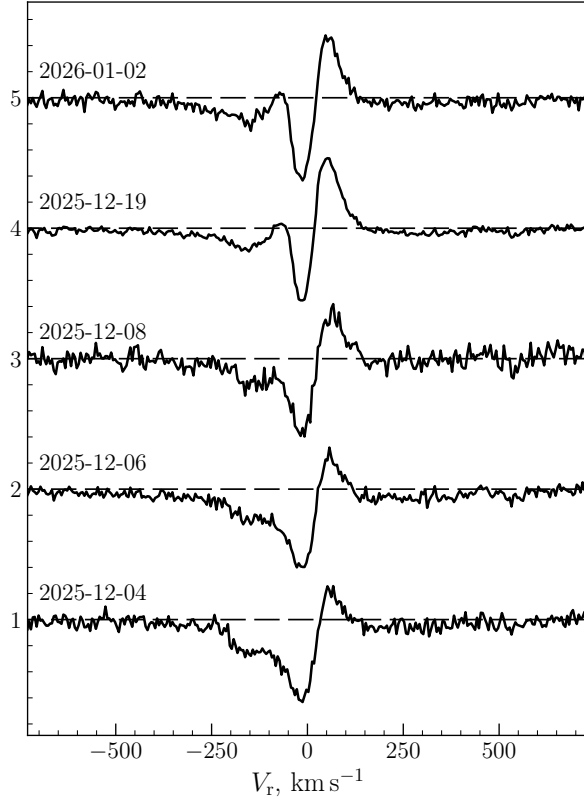


Figure 6. Evolution of the $\text{H}\alpha$ line profiles. The profiles are vertically offset by steps of 1 for clarity. The continuum level is indicated by a dashed line.

circumvent this complication and determine the stellar radial velocity V_r , we proceeded as follows.

There are at least two CTTS in the vicinity of IRAS 21204+4913, labeled as objects 1 and 2 in Fig. 1. As shown in Table 1, we obtained two spectra of the star S1 and one spectrum of the star S2. The spectra of both stars correspond to a late M spectral type, exhibit significant veiling, and display strong emission lines of hydrogen, Ca II H, K, and He I. [O I] emission line is also present in the spectrum of the S1 star (Fig. 9). For star S1, the equivalent width (EW) of $\text{H}\alpha$ line varied from 100 Å (December 20, 2025) to 55 Å (January 29, 2026). In the spectrum of the S2 star, the $\text{H}\alpha$ line exhibits a double-peaked profile with $\text{EW} \approx 53$ Å.

We have at our disposal a TDS spectrum of FN Tau – a CTTS of similar spectral type – which we used as a template for determining V_r of S1 and S2 stars. The radial ve-

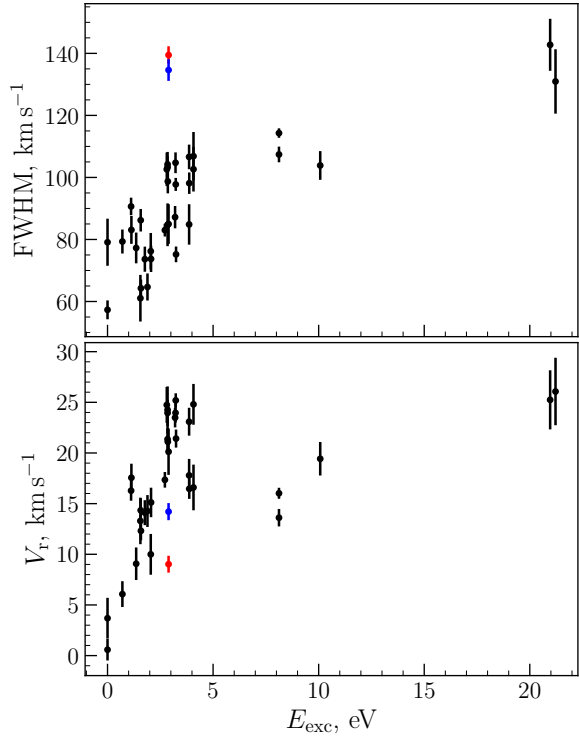


Figure 7. Dependence of the line width and barycentric radial velocity V_r on the excitation energy of the lower level of the line. The two deviating points are strong Fe II $\lambda 4923.92$ (blue) and 5018.44 Å (red) lines.

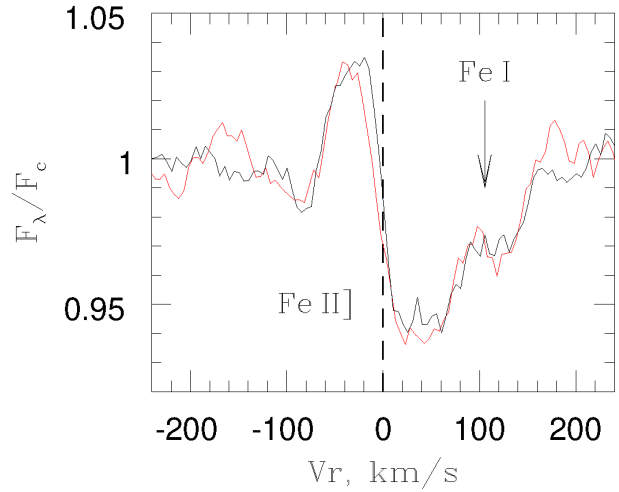


Figure 8. Profiles of the Fe II 6516.08 Å line in the spectra of IRAS 21204+4913 obtained on December 4 and 19, 2025 (red and black curves, respectively). The position of the Fe I 6518.37 Å line is indicated by an arrow.

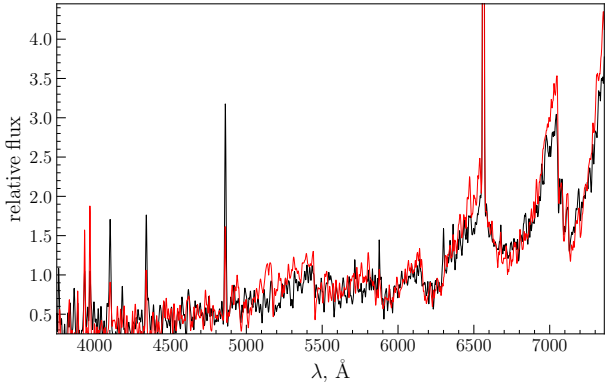


Figure 9. TDS spectra of stars S1 (black line) and S2 (red line).

lacity was measured in the wavelength range $7040 - 7300 \text{ \AA}$, where the most prominent absorption features – TiO molecular bands – are located. The observed spectra of S1 and S2 were fitted to the FN Tau template using a least-squares minimization with three free parameters: radial velocity, veiling, and a scaling factor to match the mean flux levels. After correcting for the barycentric radial velocity of FN Tau, $V_r = +15.9 \text{ km s}^{-1}$ (Jönsson et al. 2020), we obtained the following barycentric radial velocities: for S1: $V_r = -7 \pm 10 \text{ km s}^{-1}$ (December 20, 2025) and $V_r = +9 \pm 5 \text{ km s}^{-1}$ (January 29, 2026); for S2: $V_r = +14 \pm 6 \text{ km s}^{-1}$ (December 20, 2025).

According to the Gaia DR3 catalogue (Gaia Collaboration et al. 2021), both stars lie at the same distance from Earth ($d = 500 \pm 5\% \text{ pc}$) and have similar proper motions μ_α , μ_δ within the uncertainties.⁵ Based on these data, we conclude that S1, S2, and IRAS 21204+4913 are members of a compact star-forming region associated with the dark cloud D 2944. In such a scenario, the radial velocities of the stars in this region should be similar. Therefore, our estimate of $V_r \approx +6 \pm 10 \text{ km s}^{-1}$ for IRAS 21204+4913 appears reasonable.

Note that the effective temperature of young M-type stars is $< 3900 \text{ K}$ (Herczeg and Hillenbrand 2014), implying that the masses of S1 and S2 stars are less than 0.5 M_\odot (Baraffe et al. 2015).

⁵ The catalogue does not provide distance or proper motion data for IRAS 21204+4913.

3.6. Historical light curve

To investigate the long-term variability of IRAS 21204+4913, we estimated its brightness from archival photographic plates in the SAI MSU collection (see Section 2) and constructed a century-long light curve, shown in Fig. 10.

The star was first reliably detected on a photographic plate obtained on May 10, 1899 at a magnitude of $m_{\text{pg}} \approx 16^{\text{m}}$. It remained undetected thereafter until October 4, 1948, when it brightened to $m_{\text{pg}} \approx 14^{\text{m}5}$. Because IRAS 21204+4913 lies close to a dark nebula, suitable comparison stars were relatively distant, which reduced the photometric accuracy. On the night of October 6-7, 1948, eleven photographic exposures of the field were obtained over a span of six hours, allowing us to assess the precision of our visual magnitude estimates. The average uncertainty is likely $\approx 0^{\text{m}3}$.

As can be seen in Fig. 10, the star's brightness increased from October 1948 until mid-August 1949, after which it began to decline. The last detection of the star on the photographic plates occurred on November 17, 1952.

4. DISCUSSION

4.1. IRAS 21204+4913 and HH objects

The high degree of polarization of IRAS 21204+4913 and the wavelength independence of the polarization angle suggest that the polarization arises from scattering by dust. On p. 11 we will present evidence that this dust resides in an outflowing shell, that is a dusty wind. If the wind is axially symmetric, the polarization angle θ should be oriented perpendicular to the wind's symmetry axis (Dodon et al. 2019). Therefore, from Fig. 4 it follows that the position angle of the wind axis is $\text{PA}_w = \theta \pm 90^\circ = 156^\circ \pm 1^\circ$ or $-24^\circ \pm 1^\circ$.

The second value is in excellent agreement with the direction from IRAS 21204+4913 to the HH objects: $\text{PA}_{\text{HH}} \approx -25^\circ$ (see Fig. 1). We regard this alignment as strong evidence that the detected HH objects constitute part of a jet driven by the star under study. The barycentric

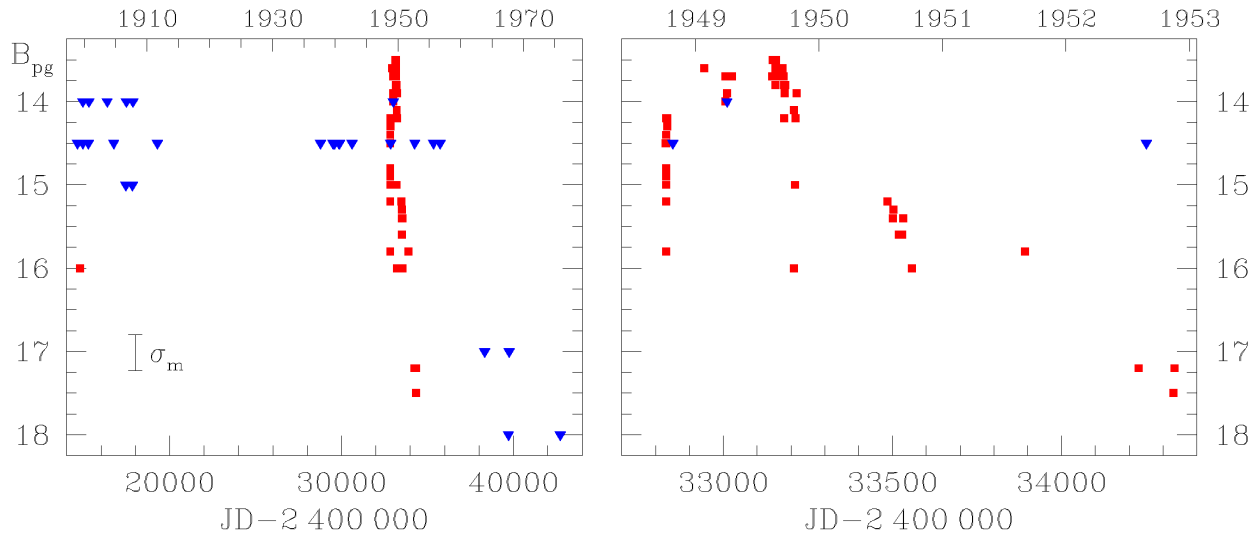


Figure 10. Left panel: Light curve of IRAS 21204+4913 constructed from measurements of archival photographic plates obtained between 1899 and 1975. The measurement uncertainty is indicated in the lower-left corner (see text). Right panel: A zoomed-in segment of the light curve around the 1948 outburst. Red squares show measured magnitudes, while blue triangles denote upper limits.

radial velocity of the star is positive, whereas the HH objects exhibit negative radial velocities – see Figs. 7 and 2, respectively. This difference implies that the HH objects are moving toward Earth while simultaneously receding from the star.

4.2. Extinction toward IRAS 21204+4913

The absorption spectrum of IRAS 21204+4913 resembles those of A-F giants and supergiants, for example, V399 Car (A9 I) and θ Sco (F1 II). This suggests that the spectral energy distribution (SED) in the optical band should also be consistent with stars of these spectral types. We compared the observed SED of IRAS 21204+4913 with the SED of A-F giants and supergiants from the catalog of Pickles (1998) and found that, under the standard interstellar extinction law ($R_V = 3.1$; Cardelli et al. 1989), the extinction A_V cannot exceed $2^m 1$ (the value $2^m 1$ is achieved for an A0 I star). For the F0 II spectrum – the closest available match to A9 I and F1 II in the catalog – we obtain $A_V = 1^m 7$.

For larger values of A_V , a kink appears near 4700 \AA , which is not observed in the spectrum of IRAS 21204+4913 (Fig. 5). The kink becomes

even more pronounced when hotter stars are used as spectral templates, ruling out the possibility of stronger reddening combined with steeper dereddened continuum for IRAS 21204+4913 than that of A-F giants. On the contrary, the presence of TiO emission bands indicates a contribution from radiation significantly cooler than that of A-F stars, which flattens the intrinsic SED by enhancing its red portion. Accounting for this cool component would lead to a lower estimate of A_V .

In the spectrum of IRAS 21204+4913 we found several diffuse interstellar bands (DIBs) from the list compiled by Herbig (1995). It is reasonable to assume that these bands arise in the portion of the dark nebula D 2944 that partially obscures the star. In particular, the EWs of the $\lambda 5797$ and 6714 \AA DIBs are measured to be 0.068 ± 0.008 and $0.097 \pm 0.012 \text{ \AA}$, respectively, with barycentric radial velocities of $V_r = -11.1 \pm 1.7$ and $-15 \pm 2 \text{ km s}^{-1}$, respectively. Using the empirical relations between the EWs of these DIBs and extinction (Lan et al. 2015), we derive A_V in the range $0^m 8 - 2^m 1$, accounting for the observed scatter in the correlations, and $A_V \approx 1^m 3$ when using the mean calibration. We also note the absence of detectable interstellar absorption in the Na I D and

KI 7699 Å lines.

On the other hand, Stecklum (2025) reports that the *Swift* observatory did not detect X-ray emission from IRAS 21204+4913 in the 0.3 – 10 keV band on November 27 and December 10, 2025, and on this basis concludes that $A_V = 8^m$. However, during our observation period the optical spectrum of the star was nearly flat (Figs. 3 and 5). If such a high extinction were applied, the dereddened luminosity in the 0.4 – 5 μm range alone would reach $\sim 10^4 L_\odot$, which is unrealistically large. This strongly suggests that the $A_V = 8^m$ estimate by Stecklum (2025) applies only to the region where the X-ray emission originates, which is obscured by the intense dusty wind as in the case of FU Ori (Skinner et al. 2010).

Thus, we adopt that the extinction in the direction of IRAS 21204+4913 $A_V \lesssim 2^m$, which is consistent with the estimate $A_V = 2^m 17 \pm 0^m 22$ for D 2944 nebula as a whole (Dobashi 2011). For such extinction, the maximum expected V band interstellar polarization would be about 5.5% (Hiltner 1956), which is much less than the observed value. Besides, interstellar polarization typically exhibits a maximum near $\lambda \approx 0.65 \mu\text{m}$. This gives reason to believe that the polarization of the object’s radiation occurs not in the interstellar medium, but in the dust shell of the star.

According to the catalog of Paegert et al. (2021), the V band magnitude of the star prior to the 2025 outburst was 19.28 ± 0.08 .⁶ Taking into account the adopted value of A_V and the distance to the star of 500 pc, this corresponds to an absolute magnitude of $M_V \approx 8^m 6$. Since eruptive YSOs are known to be younger than 10 Myr (Fischer et al. 2023), evolutionary models from Baraffe et al. (2015) imply that only stars with masses below $0.5 M_\odot$ can have absolute magnitudes fainter than this value of M_V .

4.3. Variability of the $\text{H}\alpha$ line profile

We did not observe any significant differences in the IRAS 21204+4913 spectra obtained on

different dates. The only exception is the profiles of the Balmer H I lines, especially the H α line. We already noted (Sect. 3.4) that in all our spectra, starting from December 4, the H α line has an emission component, which, however, is absent in the spectra obtained by Kochkina et al. (2025) on November 25 and 27. As can be seen from Fig. 6, the H α line displays a P Cyg profile, in which the intensity of the redshifted peak ($V_r > 0$) increases with time, and the emission component in the blue absorption wing near $V_r \approx -50 \text{ km s}^{-1}$ also strengthens. Note that Errico et al. (2003) also observed the H α profile variations in FU Ori on timescales of several days, and Powell et al. (2012) even concluded that these changes appear to be periodic.

4.4. The “redshift” effect of spectral lines

It is reliably established that the spectrum of a FUor is formed in the protoplanetary disk, whose accretion luminosity greatly exceeds the luminosity of the central star (Fischer et al. 2023). Within this framework, the presence of lines with very different excitation potentials E_{exc} in the FUor spectra is explained by the radial decrease of the effective temperature of the disk with increasing distance from the rotation axis r . Since the rotational velocity also decreases with r , the model predicts that the observed line width – e.g. the full width at half maximum (FWHM) – should be smaller for lines with lower E_{exc} (Hartmann and Kenyon 1996).

Meanwhile, Herbig (1989) already noted that, for all FUors known at the time, no dependence of FWHM on excitation energy E_{exc} was observed, at least in the visible range – see also Herbig et al. (2003), Petrov and Herbig (2008). The lack of correlation between FWHM and E_{exc} may indicate that the regions of the disk responsible for optical lines formation do not follow Keplerian rotation and/or that the FUor wind significantly distorts the observed line profiles (Petrov and Herbig 2008).

We will not discuss these reasons in further detail, because in the case of IRAS 21204+4913 a clear correlation between FWHM and E_{exc} is indeed present. Moreover, as shown in Fig. 7,

⁶ Thus, the amplitude of the outburst in the V band exceeded 8^m .

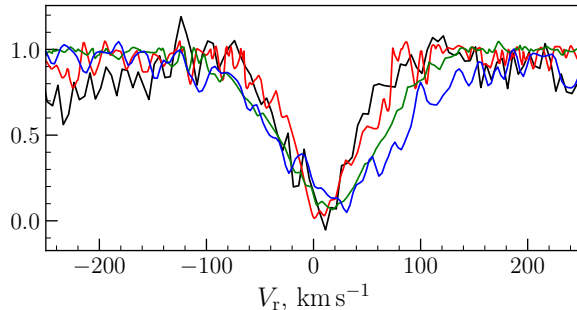


Figure 11. Dependence of the line profile shape on the excitation energy E_{exc} of the lower level. The black curve shows the Ba II 6141.71 Å line ($E_{\text{exc}} = 0.7$ eV); the red curve represents the average profile of the Sc II 5031.02, 5526.79, and 5641.00 Å lines (1.4–1.8 eV); the green curve is the average profile of the Si II 6347.11 and 6371.37 Å lines (8.1 eV); and the blue curve shows the average profile of the He I 5875.66 and 6678.16 Å lines (21 eV). Barycentric velocity is plotted along the abscissa.

the radial velocity V_r of the lines also increases with E_{exc} , a behavior not predicted by standard disk accretion models.

It can be seen from Fig. 7 that both dependencies arise because the red wing of the line becomes increasingly extended with higher E_{exc} . We believe that the change in line profiles is associated with the scattering of radiation (Grinin et al. 2012), a process whose significant role in shaping the spectrum of IRAS 21204+4913 is strongly supported by the high degree of polarization observed.

To illustrate this effect, consider a dusty wind in which the material moves radially outward at a constant velocity V_w . A photon emitted by the central star at frequency ν_0 will be Doppler-shifted in the rest frame of a dust grain to $\nu_1 = \nu_0(1 - V_w/c)$, where c is the speed of light. After a single coherent scattering event, the photon reaches the observer with frequency $\nu_2 = \nu_1(1 + V_w \cos \beta/c)$, where β is the angle between the radius vector pointing from the dust grain to the star and the line of sight. Eventually, the original wavelength λ_0 is shifted by an amount

$$\frac{\Delta\lambda}{\lambda_0} = -\frac{\Delta\nu}{\nu_0} \approx (1 - \cos \beta) \frac{V}{c} \geq 0, \quad (1)$$

toward longer wavelengths. The effects of line

shift and broadening due to *multiple* scattering are discussed in detail by Grinin et al. (2006).

The dependence of the line width on the excitation potential can be associated not only with the thermal structure of the accretion disk, but also with differences in the scattering parameters for disk regions with different temperatures. Different scattering geometries and/or scattering optical depth lead to different distortions of spectral lines. In other words, the observed spectrum depends on the geometry and kinematics of both the emitting region and the dusty wind, as well as on dust properties (Grinin et al. 2012).

Having no information on these parameters, as well as spectropolarimetric data for IRAS 21204+4913, we are forced to limit ourselves to a qualitative interpretation of the “redshift” effect.

4.5. Accretion rate estimate

The phenomenological division of eruptive YSOs into FUors and EXors, described in the Introduction, reflects fundamental differences in the accretion regimes of the protoplanetary disk’s matter onto the central star (Hartmann et al. 2016). EXors exhibit so-called magnetospheric accretion, similar to that in CTTSs, but with a much higher accretion rate \dot{M}_{ac} . For accretion rates typical of FUors ($\dot{M}_{\text{ac}} \gtrsim 10^{-5} M_{\odot} \text{yr}^{-1}$), the protoplanetary disk “pushes through” the stellar magnetic field and makes direct contact with the stellar surface. Consequently, energy is released in a boundary layer near the star rather than in an accretion shock, as is the case for EXors and CTTSs.

Fig. 12 shows the SED of IRAS 21204+4913 in the 0.4–5 μm range, uncorrected for extinction. The SED is constructed from photometric data obtained at the beginning (December 9, 2025) and the end (January 29, 2026) of our observations (see Tables A1 and A2). During this period, the total flux in the considered wavelength range increased by approximately 15 %, reaching a value of $\approx 1.1 \times 10^{-8} \text{ erg s}^{-1} \text{cm}^{-2}$. At a distance of 500 pc, this corresponds to a luminosity of $L \approx 90 L_{\odot}$.

For comparison, Fig. 12 also shows the pre-

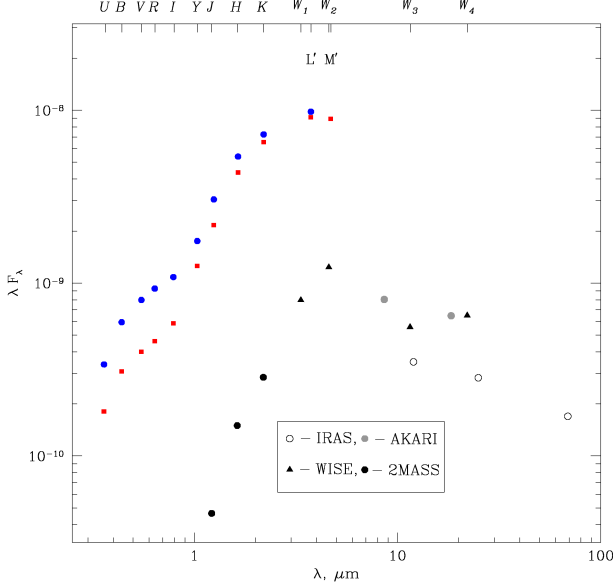


Figure 12. Temporal evolution of the SED of IRAS 21204+4913 without extinction correction. Red and blue symbols show the SED on December 9, 2025 and January 29, 2026, respectively. Pre-outburst data were obtained at different epochs and compiled from various sources; see text for details.

outburst SED of the star, constructed from archival data obtained at different epochs from the 2MASS (Skrutskie et al. 2006), WISE (Furlan et al. 2011), AKARI (Ishihara et al. 2010), and IRAS (Neugebauer et al. 1984) surveys. From these data we find that the pre-outburst bolometric luminosity of the star was $\approx 20 L_\odot$, with the range $0.4-5 \mu\text{m}$ accounting for only $\sim 10\%$. It is unlikely that the flux at wavelengths $\lambda > 5 \mu\text{m}$ remained unchanged during the outburst. Therefore, it is reasonable to assume that the bolometric luminosity during this period was at least twice the value inferred from the $\lambda < 5 \mu\text{m}$ flux alone, reaching $L_* \sim 200 L_\odot$.

If this luminosity is powered by accretion onto a star of mass M_* and radius R_* , then from the relation $L_* = \dot{M}_{\text{ac}} GM_*/R_*$ (Shakura and Sunyaev 1973) we obtain that the accretion rate at that time must have exceeded

$$\dot{M}_{\text{ac}} = 6 \times 10^{-6} \left(\frac{R_*}{R_\odot} \right) \left(\frac{M_\odot}{M_*} \right) M_\odot \text{yr}^{-1}. \quad (2)$$

According to Baraffe et al. (2015), for young stars younger than 10 Myr with masses $M_* < 0.5 M_\odot$ (see p. 10), the ratio $(R_*/R_\odot)/(M_*/M_\odot) > 5$.

Therefore, we conclude that during our observation period the accretion rate was $\gtrsim 3 \times 10^{-5} M_\odot \text{yr}^{-1}$.

4.6. Activity of the star before the 2025 outburst

Kochkina et al. (2025) found no evidence in the ASAS-SN data for strong outbursts of IRAS 21204+4913 between 2015 and October 2025. However, Stecklum (2025), relying on data from the Gaia (Mowlavi et al. 2021) and NEOWISE (Mei et al. 2023) observations, reports that before the outburst, IRAS 21204+4913 experienced long-term brightness variations of small amplitude in both the visible (after 2015) and NIR (after 2010) spectral regions. Stecklum (2025) also noted that a strong H α line was observed in the spectrum of the star before 2025 (Barentsen et al. 2014) and suggested that intense accretion of circumstellar matter was already occurring before the 2025 outburst. This is further supported by the shape of the SED (Fig. 12) and the high luminosity of the star during that period.

Finally, we note (Section 3.6) that IRAS 21204+4913 underwent a prolonged brightness increase in the past. As can be seen from Fig. 10, the star experienced an outburst in 1948, during which its brightness rose to $m_{\text{pg}} \approx 13^{\text{m}}5$, and then declined over approximately three years to a level of $m_{\text{pg}} \approx 18^{\text{m}}$. If this level represents the pre-outburst state of the star, then the amplitude of the 1948 outburst was $\Delta m_{\text{pg}} \approx 4^{\text{m}}5$.

It's difficult to say how similar the 1948 and 2025 outbursts are: we do not know what the star's spectrum was during the first outburst, how quickly its brightness increased in 1948, and how long it will continue to decline after the second outburst. Already now, IRAS 21204+4913 is approximately 2^{m} brighter in the B band than it was in 1949, however, we cannot rule out that the true maximum of the 1948 outburst was missed — see Fig. 10. Nevertheless, the very fact that an outburst of comparable amplitude occurred in an object that currently exhibits many characteristic features of a FUor is highly significant.

Herbig (1977), based on statistical grounds, concluded that the FUor phenomenon in young stars should be recurrent – see also Hillenbrand and Findeisen (2015). Meanwhile, among eruptive YSOs, considered “bonafide” FUors in the Contreras Peña et al. (2025) catalog, no confirmed cases of repeated outbursts have been observed to date. On the other hand, in a number of objects with *some* characteristic FUor-like features – for example, V1647 Ori (Aspin et al. 2009) or V899 Mon (Ninan et al. 2015) – the brightness dropped sharply a few years after the maximum, and then began to increase again. Unlike these objects, IRAS 21204+4913 had a much longer interval between outbursts – at least 77 years.

Not all mechanisms invoked to explain FUor outbursts (see Introduction) can account for this kind of phenomenon. However, some models explicitly predict the presence of “double” outbursts in FUors, e.g., Grigoryev and Demidova (2025). In this regard, we recall that in EXors, repeated prolonged outbursts are observed quite frequently – see, for example, Dodin et al. (2016), Giannini et al. (2015), Herbig (1977).

5. CONCLUSION

There is no doubt that IRAS 21204+4913 is an eruptive YSO in the transitional stage from a protostar to a young star. The object is embedded within the dark nebula D2944, which is a compact star-forming region located at a distance of approximately 500 pc and hosting low-mass YSOs ($M \lesssim 0.5 M_{\odot}$). We estimate the extinction toward IRAS 21204+4913 to be $A_V \lesssim 2^m$.

The outburst of IRAS 21204+4913, which began in late October 2025, resembles FUor-type eruptions – phenomena driven by a dramatic increase in the accretion rate of material from the protoplanetary disk onto the forming star – in several aspects:

- A large outburst amplitude ($\Delta V > 6^m$) corresponding to an accretion rate of $\gtrsim 3 \times 10^{-5} M_{\odot} \text{yr}^{-1}$;
- An absorption spectrum in the range $0.4 -$

$0.75 \mu\text{m}$ resembling those of A–F giants and supergiants, combined with the presence of TiO molecular bands;

- An outflowing shell expanding at velocities up to $\approx 300 \text{ km s}^{-1}$, in which the $\text{H}\alpha$ line with a P Cyg profile is formed;
- A group of HH objects in the vicinity of IRAS 21204+4913, receding from it with radial velocities of $V_r \approx 70 \text{ km s}^{-1}$.

At the same time, we have identified several distinctive features in IRAS 21204+4913. As the star brightened, its radiation became increasingly polarized, reaching $\approx 16\%$ in the I band by the end of our observations. We attribute this to the presence of a dusty wind. The scattering of the central source’s radiation by dust grains produces a dependence of both the FWHM and V_r of spectral lines on their excitation potential – an effect not previously observed in FUors. Another notable feature of IRAS 21204+4913 is an outburst of comparable amplitude that occurred 77 years ago.

We also discovered for the first time an emission line at $\lambda = 6516 \text{ \AA}$ and TiO molecular emission bands in the spectrum of an eruptive YSO with an absorption-dominated continuum. It is difficult to assess how critical these emission features are for understanding the outburst mechanism of IRAS 21204+4913. However, we note that the CO bands near $\lambda = 2.3 \mu\text{m}$ – typically seen in absorption in classical FUors – are observed in emission in the eruptive YSOs V1647 Ori and IRAS 06297+1021W (Connelley and Reipurth 2018), which led Contreras Peña et al. (2025) to classify them as intermediate objects between FUors and EXors.

It is still premature to classify IRAS 21204+4913 as a “bonafide” FUor, since – by definition – this group includes only objects whose brightness fades significantly over timescales of years to decades after maximum light (Samus’ et al. 2017). However, the issue is not merely one of formal classification of eruptive YSOs, but rather of understanding the physical mechanisms responsible for the diversity of their observed properties. The nontrivial features exhibited by IRAS 21204+4913 provide strong

grounds to assert that this young star warrants close attention. It would be highly desirable not only to repeat the observations presented here, but also to obtain spectropolarimetric data and to monitor the evolution of its SED at wavelengths beyond 5 μm .

ACKNOWLEDGEMENTS

We thank the staff of the CMO SAI MSU for their assistance during the observations. We are also grateful to M. R. Gilfanov, D. A. Lashin, and A. N. Tarasenkov for valuable discussions.

We gratefully acknowledge the use of data from the following databases in this work: SIMBAD (CDS, Strasbourg, France), the Astrophysics Data System (NASA, USA), the NIST Atomic Spectra Database (NIST, USA), and the Atomic Line List (University of Kentucky, USA).

The study was conducted under the state assignment of Lomonosov Moscow State University.

DATA AVAILABILITY

The results of the photographic magnitude measurements are available upon request.

F. C. Adams, C. J. Lada, and F. H. Shu, *Astrophys. J.* **312**, 788 (1987).

V. A. Ambartsumyan, *Astrophysics* **7** (4), 331 (1971).

C. Aspin, B. Reipurth, T. L. Beck, et al., *The Astrophysical Journal* **692** (2), L67 (2009).

M. Audard, P. Ábrahám, M. M. Dunham, et al., in H. Beuther, R. S. Klessen, C. P. Dullemond, and T. Henning (eds.), *Protostars and Planets VI*, pp. 387–410 (2014).

J. Bae, L. Hartmann, Z. Zhu, and R. P. Nelson, *The Astrophysical Journal* **795** (1), 61 (2014).

I. Baraffe, V. G. Elbakyan, E. I. Vorobyov, and G. Chabrier, *Astron. and Astrophys.* **597**, A19 (2017).

I. Baraffe, D. Homeier, F. Allard, and G. Chabrier, *Astron. and Astrophys.* **577**, A42 (2015).

G. Barentsen, H. J. Farnhill, J. E. Drew, et al., *Monthly Notices Royal Astron. Soc.* **444** (4), 3230 (2014).

A. A. Belinski, A. V. Dodin, S. G. Zheltoukhov, et al., *Astrophysical Bulletin* **78** (3), 283 (2023).

L. N. Berdnikov, A. A. Belinskii, N. I. Shatskii, et al., *Astronomy Reports* **64** (4), 310 (2020).

A. S. Bolton and D. J. Schlegel, *Publ. Astron. Soc. Pacific* **122** (888), 248 (2010).

E. M. A. Borchert, D. J. Price, C. Pinte, and N. Cuello, *Monthly Notices Royal Astron. Soc.* **517** (3), 4436 (2022).

J. A. Cardelli, G. C. Clayton, and J. S. Mathis, *Astrophys. J.* **345**, 245 (1989).

J. L. Clem and A. U. Landolt, *Astron. J.* **152** (4), 91 (2016).

M. S. Connelley and B. Reipurth, *Astrophys. J.* **861** (2), 145 (2018).

C. Contreras Peña, J. Lee, G. Herczeg, and J. Doug, *Journal of The Korean Astronomical Society* **58**, 209 (2025).

T. V. Demidova and V. P. Grinin, *The Astrophysical Journal* **953** (1), 38 (2023).

K. Dobashi, *Publ. Astron. Soc. Japan* **63**, S1 (2011).

A. Dodin, K. Grankin, S. Lamzin, et al., *Monthly Notices Royal Astron. Soc.* **482** (4), 5524 (2019).

A. V. Dodin, N. V. Emelyanov, A. V. Zharova, et al., *Astronomy Letters* **42** (1), 29 (2016).

A. V. Dodin, S. A. Lamzin, and G. A. Chuntonov, *Astronomy Letters* **38** (3), 167 (2012).

L. Errico, A. Vittone, and S. A. Lamzin, *Astronomy Letters* **29**, 105 (2003).

W. J. Fischer, L. A. Hillenbrand, G. J. Herczeg, et al., in S. Inutsuka, Y. Aikawa, T. Muto, et al. (eds.), *Protostars and Planets VII, Astronomical Society of the Pacific Conference Series*, vol. 534, p. 355 (2023).

E. Furlan, K. L. Luhman, C. Espaillat, et al., *The Astrophysical Journal Supplement Series* **195** (1), 3 (2011).

Gaia Collaboration, A. G. A. Brown, A. Vallenari, et al., *Astron. and Astrophys.* **649**, A1 (2021).

T. Giannini, S. Antoniucci, B. Nisini, et al., *Astrophys. J.* **814** (1), 52 (2015).

V. V. Grigoryev and T. V. Demidova, *Astronomy Letters* **51** (5), 310 (2025).

V. P. Grinin, A. S. Mitskevich, and L. V. Tamborvtseva, *Astronomy Letters* **32** (2), 110 (2006).

V. P. Grinin, L. V. Tamborvtseva, and G. Weigelt, *Astron. and Astrophys.* **544**, A45 (2012).

N. Grosso, J. Kastner, K. Hamaguchi, and M. Richmond, *The Astronomer's Telegram* **17546**, 1 (2025).

L. Hartmann, G. Herczeg, and N. Calvet, *Annual Rev. Astron. Astrophys.* **54**, 135 (2016).

L. Hartmann and S. J. Kenyon, *Annual Rev. Astron. Astrophys.* **34**, 207 (1996).

G. H. Herbig, *Astrophys. J.* **196**, 129 (1975).

G. H. Herbig, *Astrophys. J.* **217**, 693 (1977).

G. H. Herbig, in B. Reipurth (ed.), *European Southern Observatory Conference and Workshop Proceedings, European Southern Observatory Conference and Workshop Proceedings*, vol. 33, pp. 233–246 (1989).

G. H. Herbig, *Annual Rev. Astron. Astrophys.* **33**, 19 (1995).

G. H. Herbig, P. P. Petrov, and R. Duemmler, *Astrophys. J.* **595** (1), 384 (2003).

G. J. Herczeg and L. A. Hillenbrand, *Astrophys. J.* **786**, 97 (2014).

L. A. Hillenbrand and K. P. Findeisen, *The Astrophysical Journal* **808** (1), 68 (2015).

W. A. Hiltner, *Astrophys. J. Suppl.* **2**, 389 (1956).

D. Ishihara, T. Onaka, H. Kataza, et al., *Astron. and Astrophys.* **514**, A1 (2010).

H. Jönsson, J. A. Holtzman, C. Allende Prieto, et al., *Astron. J.* **160** (3), 120 (2020).

K. Kadam, E. Vorobyov, Z. Regály, et al., *Astrophys. J.* **895** (1), 41 (2020).

V. Y. Kochkina, M. I. Chazov, A. I. Kolbin, et al., *The Astronomer's Telegram* **17519**, 1 (2025).

A. Kramida, Yu. Ralchenko, J. Reader, and NIST ASD Team, NIST Atomic Spectra Database (ver. 5.12), [Online]. Available: <https://physics.nist.gov/asd> [2026, January 11]. National Institute of Standards and Technology, Gaithersburg, MD. (2024).

C. J. Lada, *Progress of Theoretical Physics Supplement* **158**, 1 (2005).

T.-W. Lan, B. Ménard, and G. Zhu, *Monthly Notices Royal Astron. Soc.* **452** (4), 3629 (2015).

G. Marton, L. V. Tóth, R. Paladini, et al., *Monthly Notices Royal Astron. Soc.* **458** (4), 3479 (2016).

Y. Mei, S.-M. Song, J.-T. Liu, et al., *Astrophys. J. Suppl.* **264** (2), 38 (2023).

D. M.-A. Meyer, E. I. Vorobyov, R. Kuiper, and W. Kley, *Monthly Notices Royal Astron. Soc.* **464** (1), L90 (2017).

N. Mowlavi, L. Rimoldini, D. W. Evans, et al., *Astron. and Astrophys.* **648**, A44 (2021).

A. E. Nadjip, A. M. Tatarnikov, D. W. Toomey, et al., *Astrophysical Bulletin* **72**, 349 (2017).

S. Nayakshin, J. E. Owen, and V. Elbakyan, *Monthly Notices Royal Astron. Soc.* **523** (1), 385 (2023).

G. Neugebauer, H. J. Habing, R. van Duinen, et al., *Astrophys. J.* **278**, L1 (1984).

J. P. Ninan, D. K. Ojha, T. Baug, et al., *Astrophys. J.* **815** (1), 4 (2015).

M. Paegert, K. G. Stassun, K. A. Collins, et al., arXiv e-prints arXiv:2108.04778 (2021).

F. Pepe, S. Cristiani, R. Rebolo, et al., *Astron. and Astrophys.* **645**, A96 (2021).

P. P. Petrov and G. H. Herbig, *The Astronomical Journal* **136** (2), 676 (2008).

A. J. Pickles, *Publ. Astron. Soc. Pacific* **110** (749), 863 (1998).

S. A. Potanin, A. A. Belinski, A. V. Dodin, et al., *Astronomy Letters* **46** (12), 836 (2020).

S. L. Powell, M. Irwin, J. Bouvier, and C. J. Clarke, *Monthly Notices Royal Astron. Soc.* **426** (4), 3315 (2012).

B. Proxauf, S. Öttl, and S. Kimeswenger, *Astron. and Astrophys.* **561**, A10 (2014).

B. S. Safonov, P. A. Lysenko, and A. V. Dodin, *Astronomy Letters* **43** (5), 344 (2017).

N. N. Samus', E. V. Kazarovets, O. V. Durlevich, et al., *Astronomy Reports* **61** (1), 80 (2017).

N. I. Shakura and R. A. Sunyaev, *Astron. and Astrophys.* **24**, 337 (1973).

B. J. Shappee, J. L. Prieto, D. Grupe, et al., *Astrophys. J.* **788** (1), 48 (2014).

N. Shatsky, A. Belinski, A. Dodin, et al., in I. I. Romanyuk, I. A. Yakunin, A. F. Valeev, and D. O. Kudryavtsev (eds.), *Ground-Based Astronomy in Russia. 21st Century*, pp. 127–132 (2020).

V. I. Shenavrin, O. G. Taranova, and A. E. Nadjip, *Astronomy Reports* **55** (1), 31 (2011).

S. L. Skinner, M. Güdel, K. R. Briggs, and S. A. Lamzin, *The Astrophysical Journal* **722** (2), 1654 (2010).

A. M. Skliarevskii and E. I. Vorobyov, *Astronomy Reports* **67** (12), 1401 (2023).

M. F. Skrutskie, R. M. Cutri, R. Stiening, et al., *Astron. J.* **131** (2), 1163 (2006).

D. Stamatellos, A. P. Whitworth, and D. A. Hubber, *Monthly Notices Royal Astron. Soc.* **427** (2), 1182 (2012).

B. Stecklum, *The Astronomer's Telegram* **17556**, 1 (2025).

A. M. Tatarnikov and A. A. Tatarnikov, *Moscow University Physics Bulletin* **78** (2), 221 (2023).

A. M. Tatarnikov, S. G. Zheltoukhov, N. I. Shatsky, et al., *Astrophysical Bulletin* **78** (3), 384 (2023).

A. P. Topchieva, T. S. Molyarova, and E. I. Vorobyov, *Astronomy Reports* **69** (6), 532 (2025).

S. G. Zheltoukhov, A. M. Tatarnikov, A. A. Belyakova, and E. A. Koksharova, *Moscow University Physics Bulletin* **79** (1), 97 (2024).

Z. Zhu, L. Hartmann, C. F. Gammie, et al., *The Astrophysical Journal* **713** (2), 1134 (2010).

APPENDIX

Table A1. Optical photometry for IRAS 21204+4913

Date	UT	<i>U</i>	σ_U	<i>B</i>	σ_B	<i>V</i>	σ_V	<i>R</i>	σ_R	<i>I</i>	σ_I
05.12.2025	17:21	12.51	0.22	12.56	0.02	11.95	0.02	11.47	0.02	10.77	0.01
06.12.2025	16:46	12.47	0.22	12.52	0.02	11.90	0.02	11.41	0.02	10.72	0.01
08.12.2025	17:45	12.40	0.22	12.46	0.02	11.83	0.02	11.34	0.02	10.65	0.01
09.12.2025	15:27	12.31	0.22	12.40	0.02	11.78	0.02	11.31	0.02	10.62	0.01
10.12.2025	15:14	12.16	0.22	12.26	0.02	11.64	0.02	11.16	0.02	10.47	0.01
16.12.2025	16:00	11.90	0.22	12.00	0.02	11.36	0.02	10.88	0.02	10.21	0.01
18.12.2025	16:03	11.85	0.22	11.94	0.02	11.30	0.02	10.82	0.02	10.15	0.01
19.12.2025	16:34	11.82	0.22	11.92	0.02	11.28	0.02	10.80	0.02	10.14	0.01
20.12.2025	16:15	11.75	0.22	11.86	0.02	11.22	0.02	10.75	0.02	10.10	0.01
21.12.2025	15:42	11.69	0.22	11.82	0.02	11.20	0.02	10.72	0.02	10.08	0.01
23.12.2025	15:04	11.72	0.22	11.81	0.02	11.18	0.02	10.69	0.02	10.05	0.01
25.12.2025	16:40	11.66	0.22	11.75	0.02	11.11	0.02	10.63	0.02	10.00	0.01
02.01.2026	15:59	11.57	0.22	11.65	0.02	11.00	0.02	10.52	0.02	9.90	0.01
03.01.2026	14:53	11.54	0.22	11.64	0.02	11.01	0.02	10.53	0.02	9.90	0.01
04.01.2026	17:01	11.57	0.22	11.66	0.02	11.02	0.02	10.54	0.02	9.92	0.01
07.01.2026	14:55	11.60	0.22	11.69	0.02	11.04	0.02	10.57	0.02	9.94	0.01
12.01.2026	16:10	11.57	0.22	11.60	0.02	10.95	0.02	10.48	0.02	9.85	0.01
15.01.2026	16:49	11.60	0.22	11.64	0.02	11.01	0.02	10.51	0.02	9.90	0.01
20.01.2026	15:10	11.59	0.22	11.61	0.02	10.95	0.02	10.47	0.02	9.84	0.01
21.01.2026	15:16	11.58	0.22	11.62	0.02	10.97	0.02	10.49	0.02	9.88	0.01
28.01.2026	15:32	11.63	0.22	11.68	0.02	11.04	0.02	10.56	0.02	9.93	0.01
29.01.2026	15:24	11.63	0.22	11.69	0.02	11.03	0.02	10.55	0.02	9.95	0.01

Table A2. IR photometry for IRAS 21204+4913

Date	UT	<i>Y</i>	σ_Y	<i>J</i>	σ_J	<i>H</i>	σ_H	<i>K</i>	σ_K	<i>L'</i>	σ_L	<i>M'</i>	σ_M
05.12.2025	17:10									3.48	0.02	2.87	0.02
06.12.2025	14:40									3.46	0.02	2.77	0.05
09.12.2025	19:05	9.2	0.1	8.10	0.07	6.62	0.04	5.32	0.04	3.35	0.05	2.67	0.04
25.12.2025	19:10			8.00	0.06	6.52	0.05	5.18	0.02	3.18	0.04	2.40	0.05
03.01.2026	14:40									3.19	0.02	2.37	0.03
07.01.2026	14:20							5.04	0.10	3.28	0.04	2.55	0.06
29.01.2026	16:00	8.84	0.02	7.73	0.02	6.39	0.03	5.21	0.02	3.27	0.04	2.52	0.04

Table A3. Polarimetric results for IRAS 21204+4913 in the *B*, *V*, *R*_c, *I*_c bands.

Date	UT	p_B	σ_p	θ_B	σ_θ	p_V	σ_p	θ_V	σ_θ	p_R	σ_p	θ_R	σ_θ	p_I	σ_p	θ_I	σ_θ
dd.mm.yyyy	hh:mm	%	%	°	°	%	%	°	°	%	%	°	°				
04.12.2025	18:35													13.85	0.17	65.3	0.7
09.12.2025	16:17					7.26	0.19	65.0	1.5	8.10	0.20	64.0	1.4	13.96	0.16	65.2	0.7
18.12.2025	18:04					8.74	0.17	66.1	1.1	9.42	0.17	65.6	1.1	15.02	0.17	66.4	0.6
21.12.2025	16:30					9.25	0.17	66.1	1.0	9.97	0.17	65.6	1.0	15.68	0.16	66.5	0.6
03.01.2026	14:57					9.41	0.17	70.2	1.0	10.39	0.22	68.2	1.2	15.86	0.16	68.2	0.6
07.01.2026	15:06	8.61	0.23	66.8	1.6	9.67	0.18	68.4	1.0	10.66	0.17	68.3	0.9	15.53	0.18	66.6	0.7